

LARGE BODIES IN THE KUIPER BELT

Chadwick A. Trujillo¹

Institute for Astronomy, 2680 Woodlawn Drive, Honolulu, HI 96822
 chad@ifa.hawaii.edu

Jane X. Luu

Leiden Observatory, PO Box 9513, 2300 RA Leiden, The Netherlands
 luu@strw.leidenuniv.nl

Amanda S. Bosh

Lowell Observatory, 1400 W. Mars Hill Road, Flagstaff, AZ 86001-4499
 amanda@lowell.edu

and

James L. Elliot

Department of Earth, Atmospheric, and Planetary Sciences and Department of Physics,
 Massachusetts Institute of Technology, Cambridge, MA 02139; and Lowell Observatory,
 Flagstaff, AZ 86001
 jle@mit.edu

ABSTRACT

We present a survey for bright Kuiper Belt Objects (KBOs) and Centaurs, conducted at the Kitt Peak National Observatory (KPNO) 0.9 m telescope with the KPNO 8k Mosaic CCD. The survey imaged 164 sq deg near opposition to a limiting red magnitude of 21.1. Three bright KBOs and one Centaur were found, the brightest KBO having red magnitude 19.7, about 700 km in diameter assuming a dark Centaur-like 4% albedo. We estimate the power-law differential size distribution of the Classical KBOs to have index $q = 4.2_{-0.3}^{+0.4}$, with the total number of Classical KBOs with diameters larger than 100 km equal to $4.7_{-1.0}^{+1.6} \times 10^4$. Additionally, we find that if there is a maximum object size in the Kuiper Belt, it must be larger than 1000 km in diameter. By extending our model to larger size bodies, we estimate that 30_{-12}^{+16} Charon-sized and $3.2_{-1.7}^{+2.8}$ Pluto-sized Classical KBOs remain undiscovered.

Subject headings: comets: general — Kuiper Belt, Oort Cloud — solar system: formation

¹Now at California Institute of Technology, MS 150-21, Pasadena, CA 91125. chad@gps.caltech.edu

1. Introduction

The region beyond Neptune is populated by $\sim 10^5$ Kuiper Belt Objects (KBOs) with diameter $D > 100$ km, with a total mass of ~ 0.2 Earth masses (Jewitt, Luu, & Trujillo 1998). These bodies are found in three dynamical classes: (1) the Classical KBOs, which have semimajor axes in the $41 \text{ AU} < a < 47 \text{ AU}$ range with low eccentricities, $e < 0.15$; (2) the Resonant KBOs, which occupy the mean-motion resonances with Neptune, predominantly the Plutinos ($a \approx 39.4$ AU) and the 2:1 objects ($a \approx 47.7$ AU); and (3) the Scattered KBOs, which are distant ($a > 50$ AU) and have highly eccentric orbits ($e \sim 0.6$; Jewitt & Luu 2000). To date, very little is known about the physical properties of these numerous Kuiper Belt Objects (KBOs) because most of the known objects are quite faint; the known KBOs have median red magnitude $m_R \approx 23.0$. Studies of other outer Solar System objects suggest that bright ($m_R < 20$) bodies are ideal targets for physical studies (Brown et al. 1997; Luu & Jewitt 1998; Brown, Cruikshank & Pendleton 1999; Luu, Jewitt & Trujillo 2000; Brown 2000). They may also allow (1) albedo measurements through the use of combined thermal and visible measurements, as collected from Centaur 10199 Chariklo (provisional designation 1997 CU₂₆; Jewitt & Kalas 1998; Altenhoff, Menten & Bertoldi 2001) and KBO 2000 WR₁₀₆ (Jewitt & Aussel 2001); and (2) direct imaging with the Hubble Space Telescope, such as performed on Pluto (Stern, Buie & Trafton 1997) and Centaur 2060 Chiron (Parker et al. 1997). Large KBOs offer higher chances for occultations and longer duration events, such as have been observed for Chiron (Elliot et al. 1995; Bus et al. 1996), Charon (Walker 1980; Elliot & Young 1991), and Pluto (Elliot et al. 1989; Millis et al. 1993).

Very few surveys have been sensitive to these bright KBOs, primarily due to the fact that the surface density of ecliptic KBOs at $m_R \sim 20$ is low, about 1 per 100 sq deg (Ferrin et al. 2001; Larsen et al. 2001; and Trujillo, Jewitt & Luu, 2001). In the past, photographic plate surveys have been used to search for these objects. Tombaugh (1961) examined about 20,000 sq deg in a decade-long survey to visual magnitude $m_V \sim 15.5$, and found only Pluto in 1930. Kowal (1989) searched 6400 sq deg to visual magnitude $m_V \sim 20$ and found one Centaur, 2060 Chiron, but no KBOs. Although plates easily image large areas, they suffer from poor sensitivity and surface defects. In addition, computer-assisted analysis of plates is more difficult than that of charge-coupled devices (CCDs). More recently, CCDs, which have a much higher quantum efficiency than photographic plates, have played a growing role, due to technological advancements allowing increased detector size. For a review of all published wide-field (> 50 sq deg) CCD surveys, see Table 1.

In this work we report results from a new survey of the outer solar system undertaken at the Kitt Peak National Observatory (KPNO) using a large format Mosaic CCD array

(Muller et al. 1998). We have surveyed 164 square degrees to limiting red magnitude $m_{R50} = 21.1$ (defined as the magnitude at which survey efficiency drops to 1/2 the maximum value). This survey yielded 3 bright KBOs and 1 Centaur, the brightest KBO being $m_R = 19.7$, corresponding to a diameter of 710 km, assuming a 4% red albedo. We use these data to constrain the number of large KBOs and place limits on the maximum size of the KBOs using a realistic model of the discovery process.

2. Survey Data

Observations were made with the now decommissioned KPNO 0.9 m f/7.5 telescope and the 8192 x 8192 pixel Mosaic CCD array. This array is composed of eight 4096×2048 pixel CCDs, each with an independent bias level and flat-field response. Observations were made through a standard Johnson R filter to enhance the detection of the KBOs, which have $V - R \sim 0.6$. The plate scale was $0.43''/\text{pixel}$ for the $15 \mu\text{m}$ pixels, corresponding to a 0.96 sq deg field of view. This telescope and camera combination was unique in providing a nearly 1 sq deg field of view while simultaneously Nyquist-sampling stellar images. In addition, the chips were relatively free from defects and had typical quantum efficiencies of ~ 0.85 in R . Telescope and detector parameters are listed in Table 2. Fields were chosen to be within 1.5 hours of opposition where the parallactic motion of the KBOs is greatest ($\sim 3''/\text{hr}$), and easily distinguishable from the main-belt asteroid motion ($\gtrsim 25''/\text{hr}$). Nearly all ($\sim 90\%$) of the fields were confined to be within 5 deg of the ecliptic, as depicted in Figures 1 and 2. Each field was imaged three times, using 200 s exposures with a ~ 1 hour separation between images. The observed fields included in the survey passed two quality tests: (1) they must have been taken during photometric conditions, and (2) they must have had a characteristic stellar Full-Width at Half-Maximum (FWHM) better than $2.5''$. Of the 285 fields imaged in the survey, only 171 passed these criteria. These fields are listed in Table 3. As detailed in Table 2, 1998 SN₁₆₅ was discovered by Spacewatch three nights before we serendipitously detected the object. We verified that no known objects remained undiscovered in our data by computing the ephemerides of all bright ($m_V < 22.5$) objects with opposition motion slower than 10 arcsec/hr for the epochs observed.

The width, ellipticity, and position angle of the Point Spread Function (PSF) varied significantly over the Mosaic CCD field of view. We quantified this variation by fitting an elliptical Moffat PSF (Moffat 1969) to stars in the linear flux regime of the CCDs for a large number of images. Figure 3 shows the variations in the FWHM of the PSF minor axis, as measured by IRAF's IMEXAM procedure. The ellipticity was found to be correlated with the minor axis FWHM, ranging in magnitude from 0.1 – 0.3 over the focal plane.

The width, ellipticity and position angle information was used to add simulated KBOs to the data in order to test our Moving Object Detection Software (MODS, Trujillo & Jewitt 1998).

The seeing in the survey varied from $0.9''$ to $2.4''$, with median $1.5''$. We tested MODS with 3 groups of images based on the seeing ($0.9''$ – $1.4''$, $1.4''$ – $1.9''$, and $1.9''$ – $2.4''$; with median seeing $1.3''$, $1.6''$, and $2.1''$, respectively). Artificial moving objects, with profiles matched to the characteristic PSF for each image group and location in the focal plane, were added to flattened images. A tally of objects was recorded, and the detection efficiency (Figure 4) was computed and found to be uniform with respect to sky-plane speed in the 1.5 – $10''/\text{hr}$ range.

The PSF- and seeing-corrected efficiency function was fitted with the same hyperbolic tangent function used in Trujillo, Jewitt & Luu (2000), given by

$$\varepsilon = \frac{\varepsilon_{\max}}{2} \left(\tanh \left(\frac{m_{R50} - m_R}{\sigma} \right) + 1 \right). \quad (1)$$

The limiting red magnitude m_{R50} is the brightness where $\varepsilon = \varepsilon_{\max}/2$, with ε_{\max} defined as the maximum detection efficiency obtained for bright objects. The characteristic magnitude range over which the efficiency drops from ε_{\max} to zero is σ . The values of these parameters for each seeing range are listed in Table 4. The poorer seeing images show a drop in m_{R50} compared to those with good seeing, consistent with reduced signal-to-noise ratio. Thus, the limiting magnitude can be characterized as $m_{R50} = 21.8 - 2.5 \log(\theta)$, where θ represents the FWHM of a stellar image in arc sec. The quantity ε_{\max} varies little for the different seeing categories; even for the worst seeing, ε_{\max} is reduced by only 9% from the best seeing.

The discovery circumstances for the 4 KPNO objects appear in Table 5. Although the discovered objects were found during good seeing (Table 2), the null detection of objects in the medium and poor seeing cases is not statistically significant. Given the $\alpha = 0.66$ slope of the Cumulative Luminosity Function (§ 3) and the limiting magnitude and sky area presented in Table 4, 46% of the objects should be found during good seeing. Thus, the probability of all 4 object detections occurring by chance during good seeing is $0.46^4 = 4.4\%$ (less probable than a 2σ Gaussian event). We therefore combine the data for all seeing cases into a single global efficiency function.

3. The Kuiper Belt

The four critical quantities we estimate for the KBOs are: (1) the Cumulative Luminosity Function, or CLF, (2) the size distribution and total number of objects, (3) the

KBO maximum size, and (4) the total number and mass of large KBOs ($\gtrsim 2000$ km and $\gtrsim 1000$ km diameter).

3.1. The Cumulative Luminosity Function

The Cumulative Luminosity Function (CLF) describes the surface density of KBOs near the ecliptic (Σ) versus limiting red survey magnitude (m_R) and is fit by the equation

$$\log \Sigma = \alpha(m_R - m_0), \quad (2)$$

where α describes the slope and m_0 is the red magnitude at which $\Sigma = 1$ KBO per sq deg. Assuming heliocentric and geocentric distance and albedo independent of object size, and a differential size distribution $n(r)dr \propto r^{-q}dr$, where $n(r)dr$ describes the number of bodies with radii between r and $r + dr$, the size distribution of the KBOs can be directly measured via (Irwin et al. 1995)

$$q = 5\alpha + 1. \quad (3)$$

We estimated the CLF by combining the discovery results of the 86 KBOs found by Trujillo, Jewitt & Luu (2001, hereafter 01TJL) with the three KBOs found in our data. Although the 01TJL data dominate the total numbers of faint objects, the two surveys have found comparable numbers of bright objects. In addition, our brightest object (1999 DE₉, $m_R = 19.7$) was over a magnitude brighter than the brightest object from 01TJL (1999 CD₁₅₈, $m_R = 21.0$). These two data sets improve upon previous survey results due to discovery statistics that cover nearly a 5 magnitude range ($19.7 < m_R < 24.4$).

Since the CLF is a cumulative measure, the CLF value at a given magnitude is correlated with the CLF values at fainter magnitudes. Thus, a linear fit to the CLF will implicitly weight the bright bodies (which are counted in the bright and faint data points) to a greater degree than the faint bodies (which are only counted in the faint data points). We instead perform a maximum-likelihood fit to find α and m_0 (Gladman et al. 1998), using the efficiency function (Equation 1) and the sky area imaged (164 sq deg). It was impossible for all fields to be centered on the ecliptic due to the large sky area imaged. Thus, sky coverage was computed by weighting each field imaged by the fraction of KBOs expected at that ecliptic latitude, assuming the best-fit inclination distribution of 01TJL, a half-width of 20 deg. For our KPNO data, this correction reduces our 164 sq deg to an effective area of 95.7 sq deg, resulting in a minor change (23%) in the normalization of $\log(\Sigma)$, a factor 2 smaller than the 1σ Poisson uncertainty for $\log(\Sigma)$ due to the 4 KBOs discovered (45%). The resulting best fit follows $\alpha = 0.66 \pm 0.06$ and $m_0 = 23.32 \pm 0.09$. This result is in statistical agreement with many other previous works (Jewitt, Luu & Trujillo

1998 with $\alpha = 0.58 \pm 0.05$, $m_0 = 23.27 \pm 0.11$; Gladman et al. 1998 with $\alpha = 0.76_{-0.11}^{+0.10}$ and $m_0 = 23.40_{-0.18}^{+0.20}$; Chiang & Brown 1999 with $\alpha = 0.52 \pm 0.05$ and $m_0 = 23.5 \pm 0.06$; and 01TJL $\alpha = 0.63 \pm 0.06$, $m_0 = 23.04_{-0.09}^{+0.08}$). We present this simple fit, our observations, and other works covering > 50 sq deg in Figure 5. Using equation 3, we find the exponent of the differential size distribution to be $q = 4.3 \pm 0.3$. We present a more detailed analysis in the next section, where we use a more realistic simulation to constrain the slope of the size distribution.

3.2. The Size Distribution of the KBOs

To better constrain the size distribution, we estimate q and the total number of Classical KBOs larger than 100 km, $N_{\text{CKBOs}}(D > 100 \text{ km})$, using a more realistic maximum-likelihood simulation than the CLF fit described in the previous section. Bias factors such as the detection efficiency and the distribution of discovery distances are correctly handled in this more detailed simulation. A full description of our simulation can be found in Trujillo, Jewitt & Luu (2000) and 01TJL. We summarize the assumed quantities in Table 6, and key procedures here:

- (1) Simulated orbital elements and object sizes were drawn for the Classical KBOs (CKBOs).
- (2) Object brightnesses were computed from the following formula (Jewitt & Luu 1995):

$$m = m_{\odot} - 2.5 \log(p\Phi(\alpha')r^2) + 2.5 \log(2.25 \times 10^{16}R^2\Delta^2), \quad (4)$$

where α' represents the phase angle of the observations, $\Phi(\alpha')$ is the Bowell et al. (1989) phase function for dark bodies ($G = 0.15$), geometric albedo is given by p , object radius is described by r [km], and R [AU] and Δ [AU] describe the heliocentric and geocentric distance of the body, respectively. The apparent red magnitude of the Sun is $m_{\odot} = -27.1$.

- (3) Object ecliptic coordinates and velocities were computed from the equations of Sykes & Moynihan (1996, sign error corrected).
- (4) The observed field areas and efficiency functions were used to determine which of the simulated objects could be detected in either our survey or that of 01TJL, based on the ecliptic coordinates, velocities and brightnesses computed in steps 2 and 3.
- (5) Two tallies of the radii of the “detected” simulated objects were kept, one for our KPNO 8k Mosaic survey and one for the 01TJL survey. Steps 1-4 were repeated until there were a factor 10 to 100 more simulated objects in each radius bin than were actually

observed.

(6) The likelihood of the model producing the observed distribution of radii was estimated by assuming Poisson detection statistics with the number of “detected” simulated objects providing the expectation value for each bin. This dataset consists of the 57 CKBOs found by 01TJL, and the single CKBO found in the KPNO survey (1999 DF₉). Although the 01TJL data contains many more objects, the KPNO survey has comparable area coverage, and number of bright object discoveries.

(7) Steps 1-6 were repeated, each time varying the size distribution index, q , and the total number of Classical KBOs, $N_{\text{CKBOs}}(D > 100 \text{ km})$, with the ultimate goal of finding the number of CKBOs and size distribution that has the maximum likelihood of producing the observations.

The primary process we are modeling is the effect of heliocentric distance R and geocentric distance Δ on the apparent red magnitude m_R , and the resulting probability of detection based on detection efficiency (Equation 1) and survey area. The inclination distribution assumed in Table 6 is equivalent to the best-fit value found by 01TJL — a Gaussian model with half-width of 20 deg. The true ecliptic latitude distribution of observed fields was used in the simulation, so no explicit correction for finite belt thickness is necessary, as needed in the CLF fit (§ 3.1).

The results for the best-fit size distribution index, q , and number of Classical KBOs with diameters $D > 100 \text{ km}$, $N_{\text{CKBOs}}(D > 100 \text{ km})$, are presented in Figure 6. This figure depicts the contours of constant probability that the given q and $N_{\text{CKBOs}}(D > 100 \text{ km})$, could produce the observed distribution. We find that

$$\begin{aligned} q &= 4.2_{-0.3}^{+0.4} & (1\sigma) \text{ and} \\ &= 4.2_{-0.8}^{+1.0} & (3\sigma), \\ && \text{and} \\ N_{\text{CKBOs}}(D > 100 \text{ km}) &= 4.7_{-1.0}^{+1.6} \times 10^4 & (1\sigma) \text{ and} \\ &= 4.7_{-2.2}^{+4.0} \times 10^4 & (3\sigma). \end{aligned}$$

This estimate of q is in formal agreement with that derived from the CLF alone at $< 1\sigma$ level.

The results for q to not depend sensitively on our model assumptions. Our values for $N_{\text{CKBOs}}(D > 100 \text{ km})$ are somewhat dependent on the inclination distribution assumed, as thicker inclination distributions can hide more objects at high ecliptic latitudes where no observations were made. For example, increasing the half-width of the inclination distribution by a factor of two, from 20 deg to 40 deg results in an increase in the best-fit $N_{\text{CKBOs}}(D > 100 \text{ km})$, from 4.7×10^4 to 7.5×10^4 , a factor 1.6. The

best-fit value for $N_{\text{CKBOs}}(D > 100 \text{ km})$ is roughly linear with half-width $i_{1/2}$, following $N_{\text{CKBOs}}(D > 100 \text{ km}) \sim (1.9 + 0.14i_{1/2}) \times 10^4$.

3.3. The Maximum Size of Kuiper Belt Objects

Adopting the best-fit $q = 4.2$, we simulated the CLF that would be found by our survey given several different maximum sizes for the Classical KBOs, with results appearing in Figure 7. The expected CLF from the Classical KBOs was multiplied by the observed KBO : Classical KBO ratio (89:58) to construct this graph, which makes the implicit assumption that the CLF of the Classical KBOs matches that of the KBOs as a whole. This assumption is reasonable, as a maximum-likelihood fit to the CLF for the Classical KBOs alone ($\alpha = 0.71^{+0.07}_{-0.06}$) is statistically consistent with the fit to all observed populations ($\alpha = 0.66 \pm 0.06$, § 3.1).

Our analysis rules out the $D_{\text{max}} = 500 \text{ km}$ and $D_{\text{max}} = 250 \text{ km}$ diameter maximum sizes, as is expected since we found one body with diameter $D \sim 700 \text{ km}$ and another with $D \sim 500 \text{ km}$. The $D_{\text{max}} = 1000 \text{ km}$ simulation is the best-fit to our data, however, these data are formally consistent with all greater D_{max} . Thus, if there is a maximum size cutoff, it is greater than or equal to $D_{\text{max}} = 1000 \text{ km}$, because we do not observe a significant surface density decrease for bright objects beyond that described by the linear slope of the CLF. This analysis is in agreement with all other published wide-field surveys except for Kowal (1989). Kowal's (1989) datum could be explained by a precipitous drop in surface density between $19 < m_R < 20$, as would be expected if there were a maximum size of $D = 1000 \text{ km}$ to the KBOs. Such a model would be in violation of the Tombaugh (1961) datum point, unless Pluto is considered a special case. In either case, our observations indicate that if there is a maximum size, it must be $D_{\text{max}} \geq 1000 \text{ km}$.

3.4. The Total Number and Mass of Large Kuiper Belt Objects

The number of large KBOs is of fundamental interest because it is a direct measurement of the runaway accretion in the planet forming era of the solar system (Kenyon & Luu 1998). Two sizes of typical interest are the number of Charon-sized bodies ($\sim 1000 \text{ km}$ in diameter) and the number of Pluto-sized bodies ($\sim 2000 \text{ km}$ in diameter). The number of bodies with diameters larger than D_{min} , given by $N(D > D_{\text{min}})$, can be directly calculated

from the results of our maximum likelihood simulation. For $q \neq 1$,

$$N(D > D_{\min}) = N_{\text{CKBOS}}(D > 100 \text{ km}) \left(\frac{100 \text{ km}}{D_{\min}} \right)^{q-1}. \quad (5)$$

Thus, from Figure 6, we find that the total numbers of Charon- and Pluto-sized bodies in the Classical Kuiper Belt follow

$$\begin{aligned} N(D > 1000 \text{ km}) &= 30_{-12}^{+16} \quad (1\sigma) \text{ and} \\ &= 30_{-22}^{+57} \quad (3\sigma), \\ &\text{and} \\ N(D > 2000 \text{ km}) &= 3.2_{-1.7}^{+2.8} \quad (1\sigma) \text{ and} \\ &= 3.2_{-2.7}^{+12.2} \quad (3\sigma). \end{aligned}$$

Thus, assuming that the $q = 4.2$ size distribution continues to large sizes, we expect that there are ≥ 1 (3σ lower-limit) undiscovered Pluto-sized bodies in the Classical Kuiper Belt and ≥ 8 (3σ lower-limit) Charon-sized bodies, of which only a few have been discovered. If the size distributions of the Classical and Scattered KBOs are identical, then a similar number of bodies should be present in the Scattered Kuiper Belt, which has approximately the same number of bodies (Trujillo, Jewitt & Luu 2000). These results are consistent with the Kuiper Belt growth models of Kenyon and Luu (1998, 1999) using velocity evolution and collisional fragmentation. In these models, several Pluto-sized bodies grow concurrently in a low-mass ($\sim 10M_{\oplus}$) disk. These models have two characteristic observable parameters: (1) The size distribution of the resulting Kuiper Belt corresponds to $q \approx 4$, and (2) several large bodies are formed concurrently. Their favored model produces ~ 150 Charon-sized bodies and 1 Pluto-sized body in 36.5 Myr (Kenyon and Luu 1999a) and is roughly consistent with our observations, although no prediction is made about the subsequent destruction rates of such bodies from catastrophic collisions.

The possibility of finding these Pluto- and Charon- sized bodies can be estimated by examining the discovery conditions of other bright bodies. Table 7 lists the three KBOs to date brighter than red magnitude $m_R = 20$ that have been found in published surveys (with the exception of Pluto). These three bodies were found in the heliocentric distance range 30–39 AU. Assuming opposition observations and 4% albedo, 2000 km and 1000 km diameter bodies at these heliocentric distances would have have brightnesses $16.9 < m_R < 18.2$ and $18.4 < m_R < 19.7$, respectively, according to Equation 4. These magnitudes are within range for most time-resolved wide-field survey telescopes, however the apparent motion of these bodies, $\sim 3''/\text{hr}$, is considerably slower than $\gtrsim 25''/\text{hr}$ main-belt asteroids. Since most such observing programs are designed to find near-Earth asteroids and other high proper motion planetary bodies, plate scales and timebases

between images are not usually conducive to finding the KBOs. Thus, special observing procedures or software methods must be adopted to find the slower KBOs, as has been done by Spacewatch (Larsen et al. 2001). A time-resolved all-sky $m_R = 20.0$ magnitude survey should be able to find all the remaining Pluto- and Charon- sized bodies, as long as suitable measures are taken to detect $\sim 3''/\text{hr}$ bodies. Such a survey could be conducted with a dedicated 1 meter class telescope outfitted with a CCD camera allowing a wide-field of view, similar to the KPNO 0.9 m and 8k CCD Mosaic instrument combination used in this work.

These analyses presume that the KBOs have a 4% albedo, consistent with the Centaurs (Jewitt & Luu 2000). If the mean KBO albedo, p , departs from this value, then the radial sizes of the bodies will be affected by a factor $(p/0.04)^{-1/2}$. For a 14% albedo such as that of Chiron (Campins et al. 1995) and a 38% albedo such as found for Charon (Buie, Tholen & Wasserman 1997), this amounts to a size factor 1.9 and 3.1, respectively.

The total amount of mass in 1000 km to 2000 km diameter Classical KBOs for our best-fit $q = 4.2$ case is

$$M(1000 \text{ km} < D < 2000 \text{ km}) = 5.4 \times 10^{-3} M_{\oplus} \left(\frac{\rho}{1000 \text{ kg m}^{-3}} \right) \left(\frac{0.04}{p} \right)^{1.6}, \quad (6)$$

with ρ representing the bulk density, p denoting the albedo, and $M_{\oplus} = 6.0 \times 10^{24} \text{ kg}$. This accounts for 18% of the total mass found in $100 \text{ km} < D < 2000 \text{ km}$ bodies. Again, the Scattered KBOs may contain a similar amount of material.

4. The Centaurs

Although there is no formal International Astronomical Union definition of the Centaur population, we classify bodies whose perihelia fall between that of Jupiter and Neptune as Centaurs, similar to the Larsen et al. (2001) definition. One such Centaur was found in the KPNO 8k data (2000 EE₁₇₃). We therefore estimate the sky-plane density of Centaurs to be $1.0_{-0.8}^{+1.6} \times 10^{-2}$ (1σ) Centaurs per sq deg at our survey limiting magnitude $m_{R50} = 21.1$. This is consistent with other recent estimates of the Centaur population: Larsen et al. (2001) predict a value of 1×10^{-2} at our limiting magnitude and Sheppard et al. (2000) predict a similar surface density of 3×10^{-3} Centaurs per sq deg.

5. Summary

We have conducted a survey for KBOs and Centaurs with the KPNO 0.9 m telescope and 8k Mosaic CCD, which together provide a nearly 1 sq deg field of view, reaching red magnitude $m_R = 21.1$ in 200 s in typical seeing conditions at Kitt Peak. We detected 3 KBOs and 1 Centaur in 164 sq deg examined near the ecliptic. Combining these new data with the results of Trujillo, Jewitt & Luu (2001), we find the following results:

- (1) The Cumulative Luminosity Function slope is $\alpha = 0.66 \pm 0.06$, with 1 KBO / sq deg occurring at red magnitude $m_0 = 23.32 \pm 0.09$.
- (2) The Classical KBOs follow a $q = 4.2_{-0.3}^{+0.4}$ (1σ) differential size distribution, with the total number of Classical KBOs with diameters larger than 100 km given by $N_{\text{CKBOs}}(D > 100 \text{ km}) = 4.7_{-1.0}^{+1.6} \times 10^4$, assuming a Gaussian inclination distribution with half-width 20 deg.
- (3) No statistically significant evidence for a maximum size cutoff to the KBOs was found. However, if such a maximum diameter exists, it must have $D_{\text{max}} > 1000$ km.
- (4) Assuming the differential size distribution extends to large sizes, the total number of Classical KBOs with diameters $D \gtrsim 1000$ km and $D \gtrsim 2000$ km is 30_{-12}^{+16} and $3.2_{-1.7}^{+2.8}$, respectively (1σ). The bodies in the $1000 \text{ km} < D < 2000 \text{ km}$ diameter range account for $\sim 1/5$ of the total mass in the $100 \text{ km} < D < 2000 \text{ km}$ diameter range, representing $M(1000 \text{ km} < D < 2000 \text{ km}) = 5.4 \times 10^{-3} M_{\oplus}$, assuming a bulk density of 1000 kg m^{-3} .
- (5) The sky-plane surface density of Centaurs brighter than $m_R = 21.1$ is $1.0_{-0.8}^{+1.6} \times 10^{-2}$ (1σ) Centaurs/sq deg near the ecliptic.

We thank the National Optical Astronomy Observatories (NOAO) for granting telescope time, David Tholen for computation of the orbital elements, Amanda Sickafoose and Wyn Evans for observational assistance, David Jewitt for editorial comments, and Nigel Sharp for technical assistance at the 0.9m telescope. This work was supported in part by a NASA grant to David C. Jewitt, NASA grant NAG5-3940 to JLE and through NSF support provided to NOAO.

REFERENCES

Altenhoff, W. J., Menten, K. M., & Bertoldi, F. 2001, *A&A*, 366, L9–L12.

Bernstein, G. & Khushalani, B. 2000, *AJ*, 120, 3323–3332.

Bus, S. J. et al. 1996, *Icarus*, 123, 478.

Brown, M. E. 2000, *AJ*, 119, 977–983.

Brown, R. H., Cruikshank, D. P., Pendleton, Y. J., & Veeder, G. J. 1997, *Science*, 276, 937.

Brown, R., Cruikshank, D., & Pendleton, Y. 1999, *ApJ*, 519, L101.

Buie, M. W., Tholen, D. J., & Wasserman, L. H. 1997, *Icarus*, 125, 233–244.

Campins, H., Telesco, C. M., Osip, D. J., Rieke, G. H., Rieke, M. J., & Schulz, B. 1994, *AJ*, 108, 2318–2322.

Chiang, E. I. & Brown, M. E. 1999, *AJ*, 118, 1411–1422.

Elliot, J. L., Dunham, E. W., Bosh, A. S., Slivan, S. M., Young, L. A., Wasserman, L. H., & Millis, R. L. 1989, *Icarus*, 77, 148.

Elliot, J. L., Olkin, C. B., Dunham, E. W., Ford, C. H., Gilmore, D. K., Kurtz, D., Lazzaro, D., Rank, D. M., Temi, P., Bandyopadhyay, R. M., Barroso, J., Barrucci, A., Bosh, A. S., Buie, M. W., Bus, S. J., Dahn, C. C., Foryta, D. W., Hubbard, W. B., Lopes, D. F., & Marcialis, R. L. 1995, *Nature*, 373, 46.

Elliot, J. L., & Young, L. A. 1991, *Icarus*, 89, 244.

Ferrin, I., Rabinowitz, D., Schaefer, B., Snyder, J., Ellman, N., Vicente, B., Rengstorf, A., Depoy, D., Salim, S., Andrews, P., Bailyn, C., Baltay, C., Briceno, C., Coppi, P., Deng, M., Emmet, W., Oemler, A., Sabbe, C., Shin, J., Sofia, S., van Altena, W., Vivas, K., Abad, C., Bongiovanni, A., Bruzual, G., Della Prugna, F., Herrera, D., Magris, G., Mateu, J., Pacheco, R., Sánchez, G., Sánchez, G., Schenner, H., Stock, J., Vieira, K., Fuenmayor, F., Hernandez, J., Naranjo, O., Rosenweig, P., Secco, C., Spavieri, G., Gebhard, M., Honnecutt, H., Mufson, S., Musser, J., Pravdo, S., Helin, E., Lawrence, K. 2001, *ApJ*, 548, L243–L247.

Irwin, M., Tremaine, S., & Źytkow, A. N. 1995, *AJ*, 110, 3082–3092.

Jewitt, D. & Aussel, H. 2001, International Astronomical Union Circular 7554.

Jewitt, D. & Kalas, P. 1998, *ApJ*, 499, 103.

Jewitt, D. & Luu, J. 2000, In *Protostars and Planets IV*, eds. V. Mannings, A. Boss & S. Russell, Univ. of Arizona Press, Tucson, pp. 1201–1229.

Jewitt, D., Luu, J., & Trujillo, C. 1998, *AJ*, 115, 2125.

Kenyon, S. J. & Luu, J. X. 1998, *AJ*, 115, 2136.

Kenyon, S. J. & Luu, J. X. 1999, *AJ*, 118, 1101.

Kowal, C. 1989, *Icarus*, 77, 118.

Larsen, J. A., Gleason, A. E., Danzl, N. M., Descour, A. S., McMillan, R. S., Gehrels, T., Jedicke, R., Montani, J. L., & Scotti, J. V. 2001, *AJ*, 121, 562–579.

Luu, J. & Jewitt, D. 1996, *AJ*, 112, 2310–2318.

Luu, J. X. & Jewitt, D. C. 1998, *ApJ*, 494, L117.

Luu, J. X., Jewitt, D. C., & Trujillo, C. A. 2000, *ApJ*, 531, L151–L154.

Luu, J., Marsden, B. G., Jewitt, D., Trujillo, C. A., Hergenrother, C. W., Chen, J., & Offutt, W. B. 1997, *Nature*, 387, 573.

Millis, R. L. et al. 1993, *Icarus*, 105, 282.

Moffat, A. F. J. 1969, *A&A*, 3, 455–461.

Muller, G. P., Reed, R., Armandroff, T., Boroson, T. A., Jacoby, G. H. 1998, SPIE, 3355, 577–585.

Parker, J. Wm., Stern, S. A., Festou, M. C., A'Hearn, M. F. 1997, *AJ*, 113, 1899.

Sheppard, S. S., Jewitt, D. C., Trujillo, C. A., Brown, M. J. I., & Ashley, M. C. B. A. 2000, 120, 2687–2694.

Stern, S. A., Buie, M. W., Trafton, L. M. 1997, *AJ*, 113, 827.

Sykes, M. V. & Moynihan, P. D. 1996, *Icarus*, 124, 399

Sykes, M. V. & Walker, R. G. 1991, *Science*, 251, 777–780.

Tegler, S. C. & Romanishin, W. 1998, *Nature*, 392, 49–51.

Tegler, S. C. & Romanishin, W. 2000, *Nature*, 407, 979–981.

Tombaugh, C. 1961, in *Planets and Satellites* (G. Kuiper & B. Middlehurst, eds.), University of Chicago, Chicago, pp. 12–30.

Trujillo, C. & Jewitt, D. 1998, AJ, 115, 1680.

Trujillo, C., Jewitt, D., & Luu, J. 2000, ApJ, 529, L103–L106.

Trujillo, C., Jewitt, D., & Luu, J. 2001, submitted to the AJ. (01TJL)

Walker, A. R. 1980, MNRAS, 192, 47.

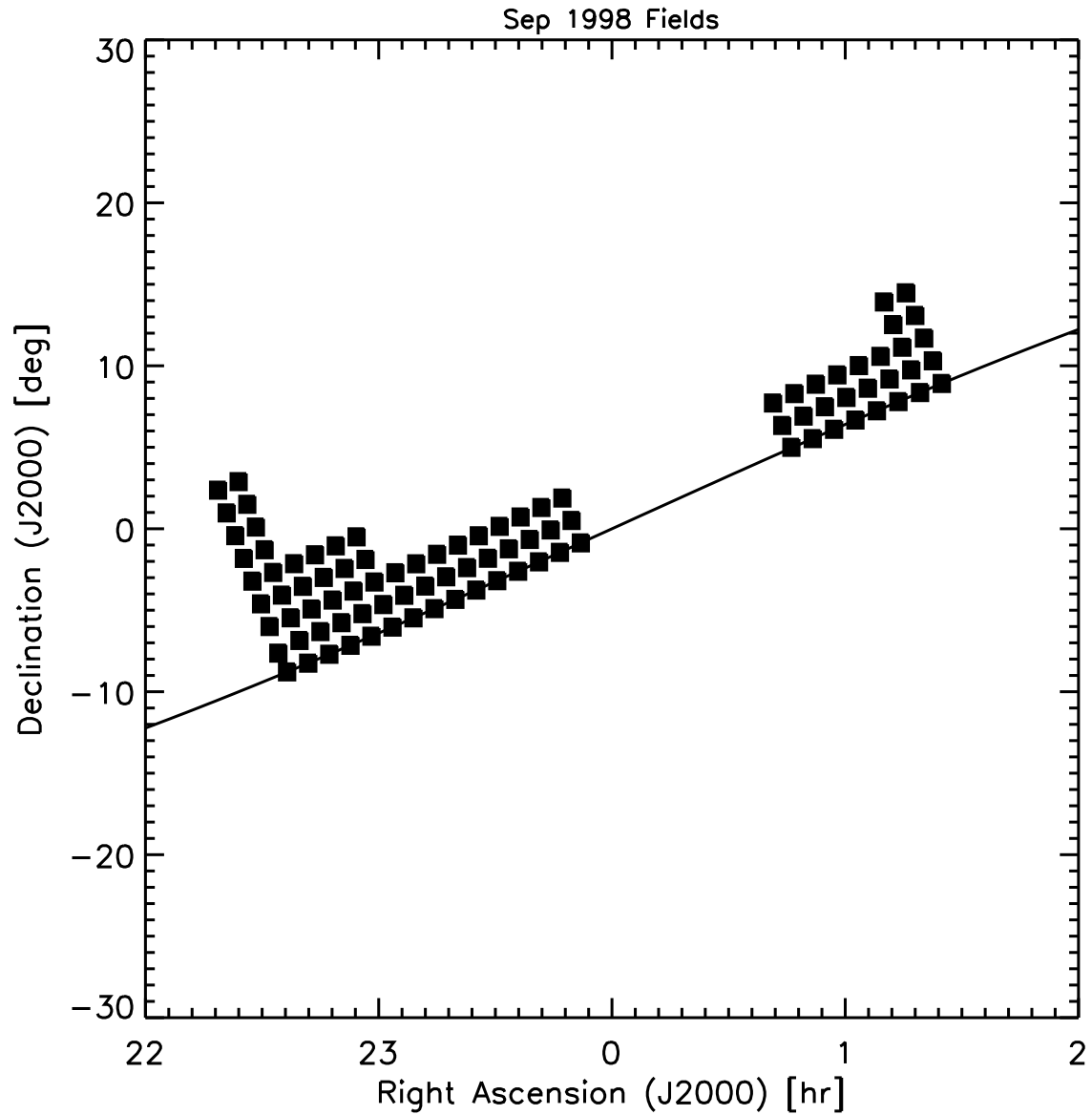


Fig. 1.— Fields that passed quality tests, imaged during Sep 1998. The ecliptic is denoted by a solid line.

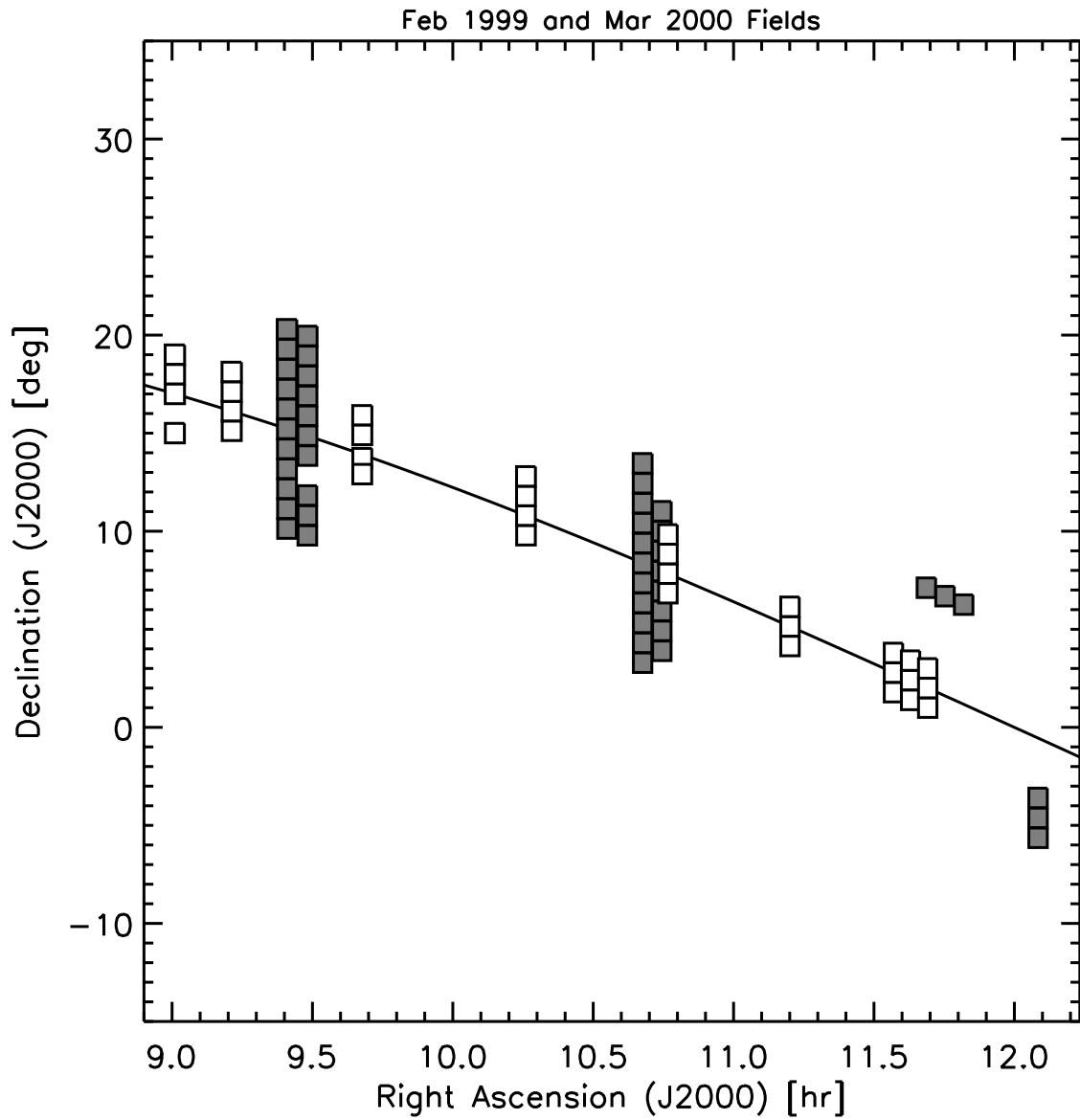


Fig. 2.— Fields that passed quality tests, imaged during Feb 1999 (white squares) and Mar 2000 (grey squares). The ecliptic is denoted by a solid line.

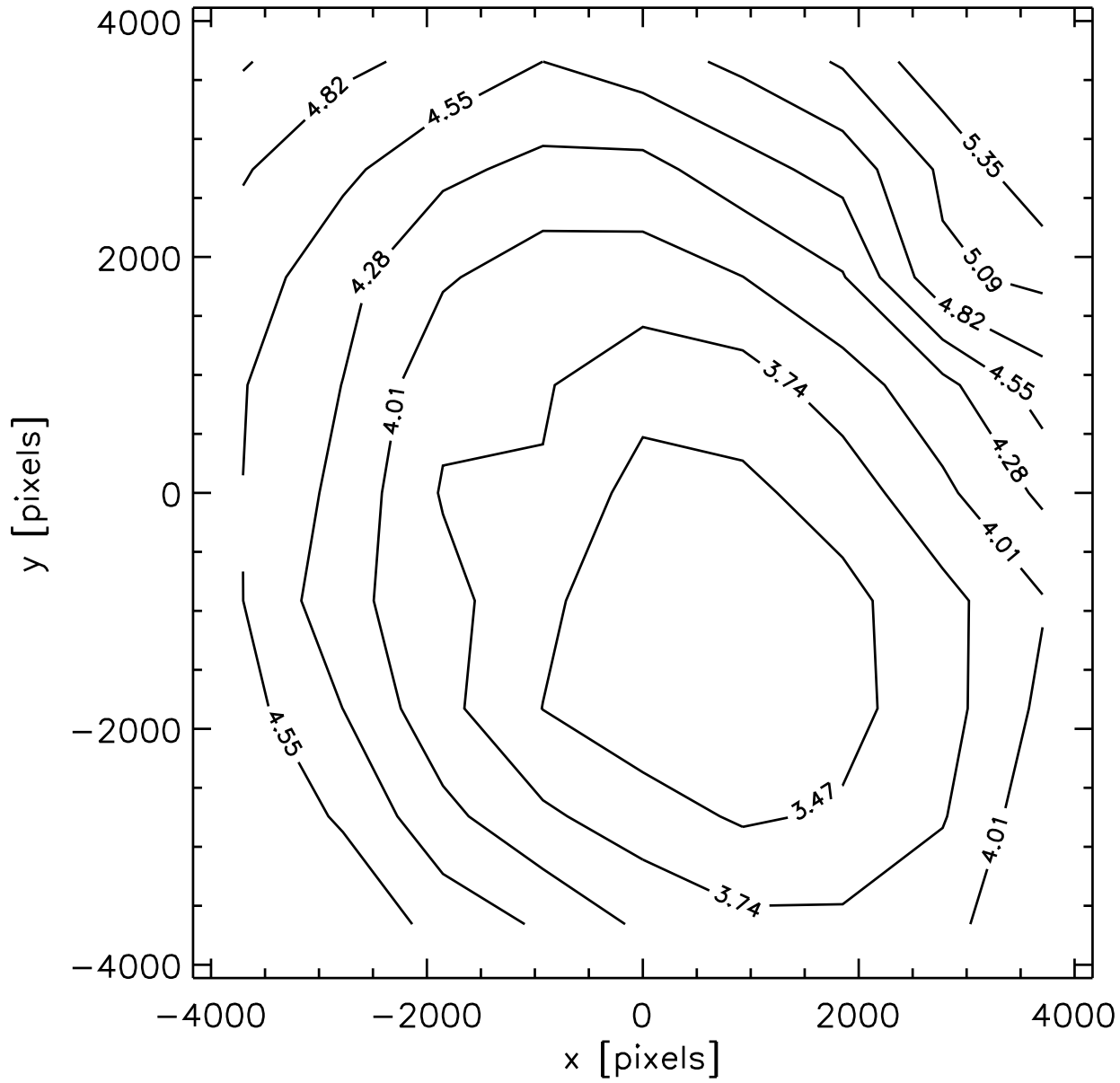


Fig. 3.— Minor axis Moffat FWHM in pixels (1 pixel = 0.43 ‐) of a stellar profile across the Mosaic CCD. Note that the chip is misaligned with the optical axis of the telescope by about 1500 pixels = 2.3 cm.

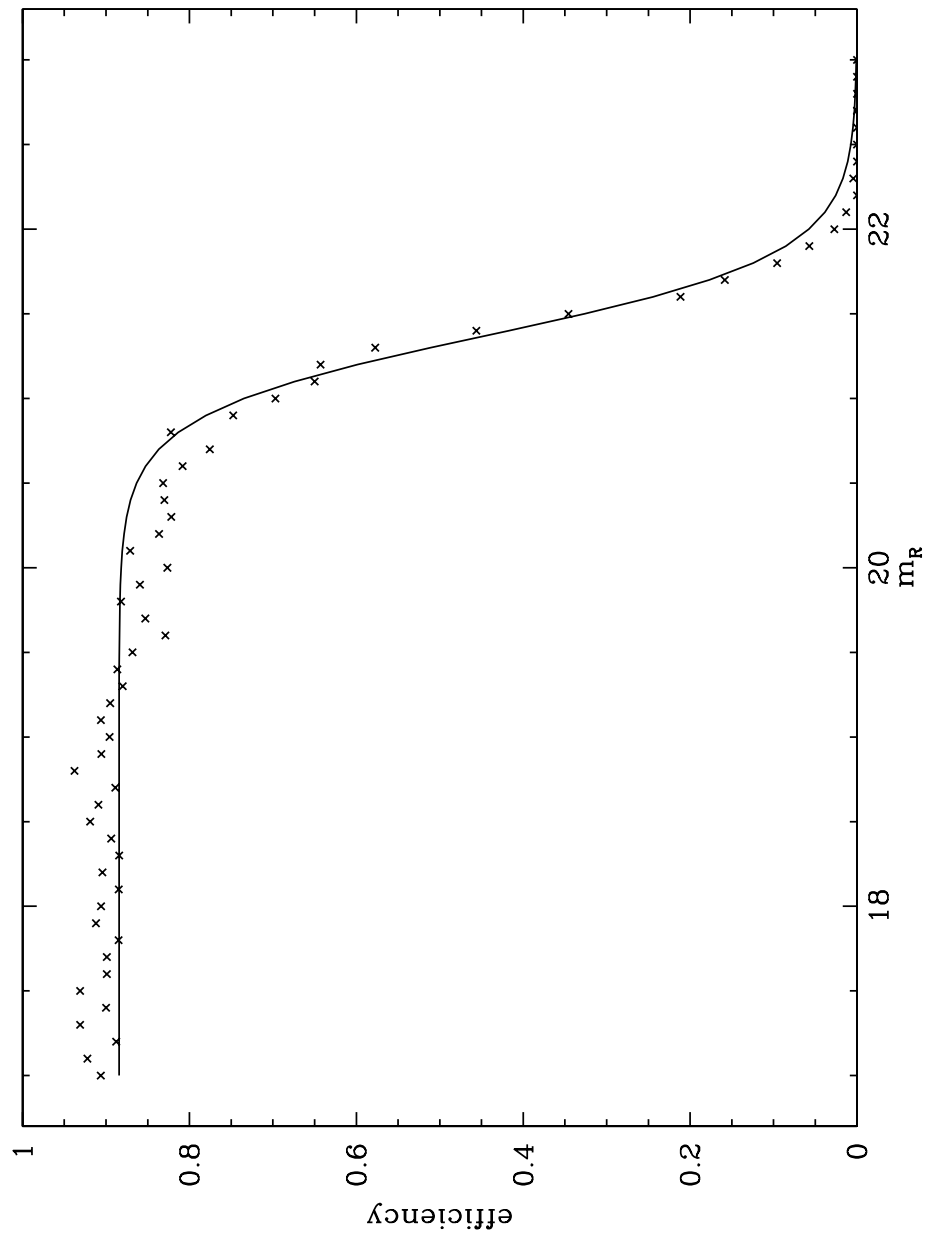


Fig. 4.— The efficiency function of the 8k CCD on the KPNO 0.9m in 1.3" seeing, with a fit to the hyperbolic tangent efficiency function.

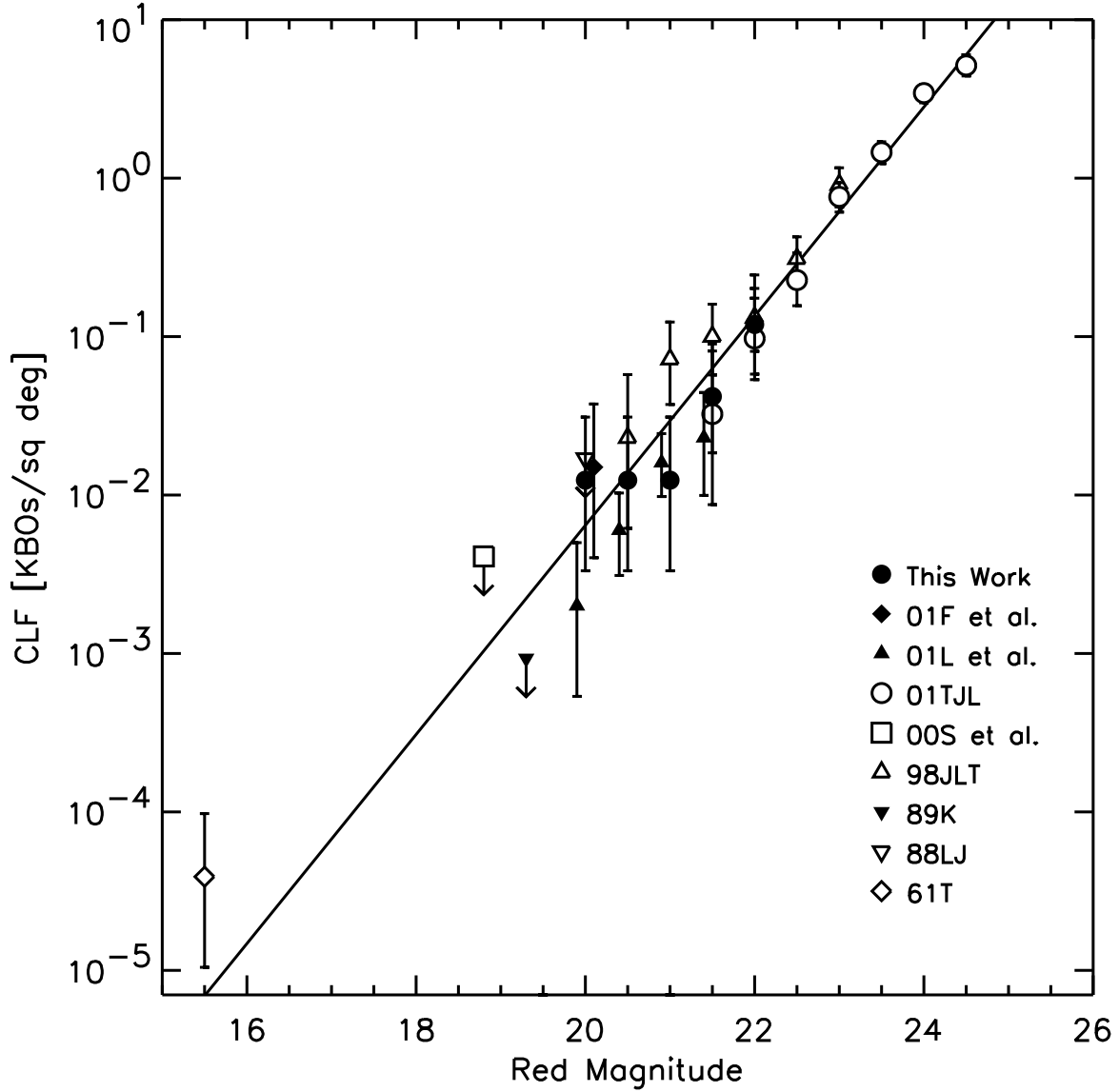


Fig. 5.— Our measurement of the Cumulative Luminosity Function (CLF), which represents the number of KBOs deg^{-2} near the ecliptic (filled circles) brighter than a given apparent red magnitude. The line represents the best fit ($\alpha = 0.66 \pm 0.06$ and $m_0 = 23.32 \pm 0.09$) to the CLF determined by this survey and that conducted by Trujillo, Luu & Jewitt (2001, 01TJL). Other points are from previous works: 01F et al. (Ferrin et al. 2001); 01L et al. (Larsen et al. 2001); 00S et al. (Sheppard et al. 2000); 98JLT (Jewitt, Luu & Trujillo 1998); 89K (Kowal 1989); 88LJ (Luu & Jewitt 1988); and 61T (Tombaugh 1961), with arrows denoting upper limits.

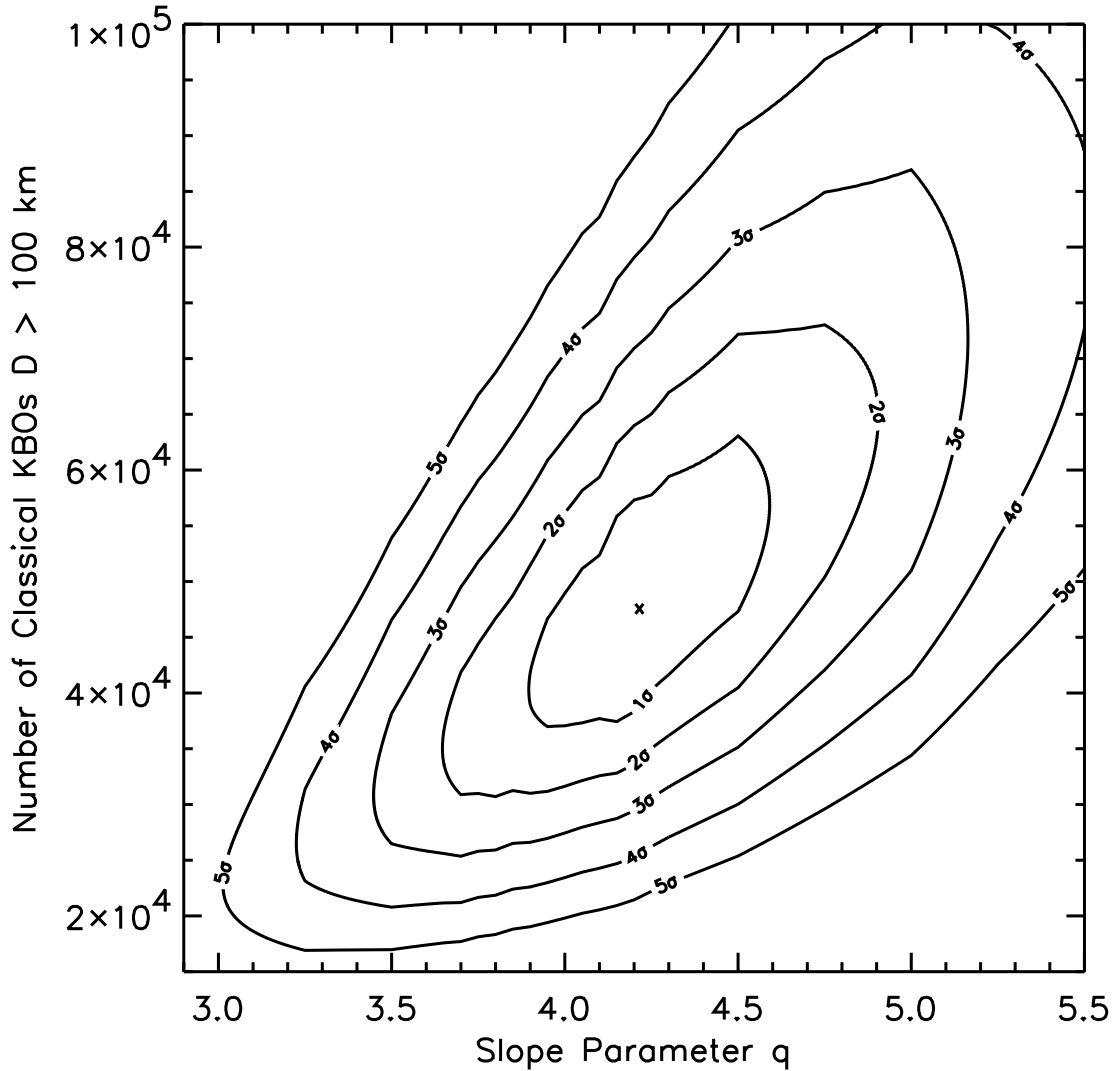


Fig. 6.— The normalized probability that the observed distribution of radii match the expected distribution given the free parameters: (1) q , the size distribution index, and (2) $N_{\text{CKBOs}}(D > 100 \text{ km})$, the total number of Classical KBOs (sigma values correspond to Gaussian confidence limits: $1\sigma = 68.3\%$, $2\sigma = 95.4\%$, etc.). The maximum likelihood occurs at $q = 4.2^{+0.4}_{-0.3}$ (1σ).

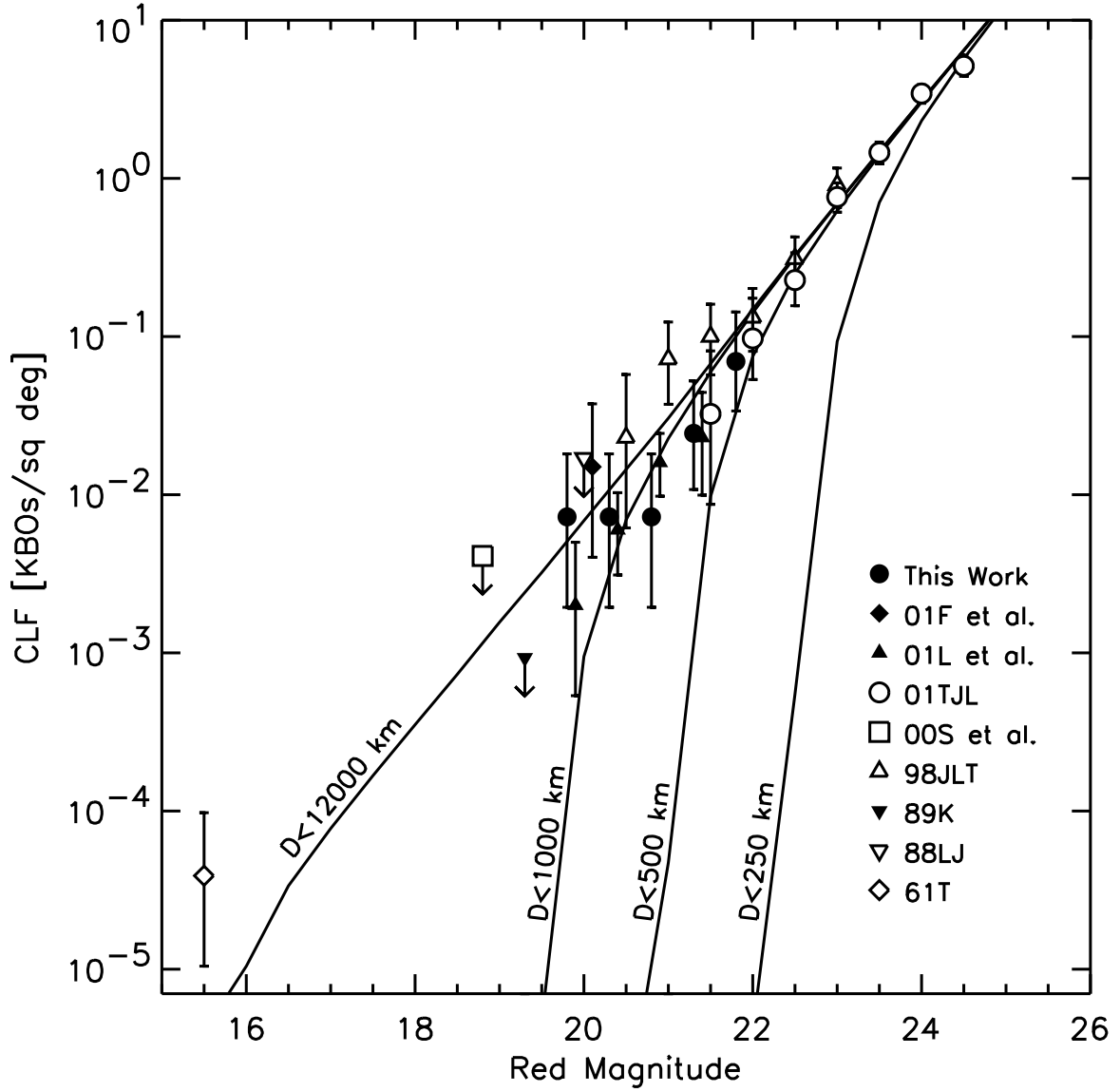


Fig. 7.— The expected observed CLF for the $q = 4.2$ case, given maximum KBO diameters (left-to-right) of 12,000 km (\sim Earth-sized), 1000 km (\sim Pluto-sized), 500 km (\sim Charon-sized) and 250 km. The 1000 km case represents the best fit, however only the 250 km and 500 km cases are rejected at the 3σ level. Formally, there is no evidence for an upper-size cutoff.

Table 1. Wide-Field CCD Surveys sensitive to KBOs

Area [sq deg]	m^a	Centaurs ^b	KBOs ^c	Brightest KBO	Source
1428	18.8 R	0 (1)	0 (0)	—	Sheppard et al. (2000)
522	20.5 V	3 (1)	7 (5)	1999 GQ ₂₁ ($m_V = 20.5$)	Larsen et al. (2001)
164	21.1 R	1 (0)	2 (1)	1999 DE ₉ ($m_R = 19.7$)	This Work
73	23.7 R	0 (0)	84 (2)	1999 CD ₁₅₈ ($m_R = 21.0$)	Trujillo, Jewitt & Luu (2001)
67	20.1 R	0 (0)	1 (0)	2000 EB ₁₇₃ ($m_R = 19.3$)	Ferrin et al. (2001)
52	22.5 R	0 (0)	13 (0)	1996 TL ₆₆ ($m_R = 20.6$)	Jewitt, Luu & Trujillo (1998)

Note. — Published CCD surveys with > 50 sq deg have been included.

^aLimiting magnitude of survey.

^bThe number of Centaurs discovered is listed, with serendipitous detections of previously discovered objects listed in parentheses.

^cThe number of KBOs discovered is listed, with serendipitous detections of previously discovered objects listed in parentheses.

Table 2. KPNO Survey Parameters

Quantity	KPNO 0.9m
Focal Ratio	f/7.5
Instrument	KPNO 8k x 8k Mosaic
Plate Scale ["/pixel]	0.43
Field Area [deg ²]	0.957
Total Fields	171
Total Area [deg ²]	164
m_{R50}^a	21.1
$\theta^b["]$	0.9–2.4
Filter	R
Quantum Efficiency	0.85

^athe red magnitude at which detection efficiency reaches half of the maximum efficiency

^brange of minor axis Full Width at Half Maximum of stellar sources near focal plane center

Table 3. CFHT Field Centers

ID	UT date	UT times	β ^a	α ^b	δ ^c	θ ^d	Objects
ecl01.12	1998 Sep 25	2:54 3:58 4:54	12	22:18:41	02:22:01	p	
ecl01.11	1998 Sep 25	3:00 4:04 5:00	10	22:20:54	00:58:19	p	
ecl01.09	1998 Sep 25	3:06 4:10 5:07	9	22:23:06	-00:25:24	p	
ecl01.08	1998 Sep 25	3:13 4:16 5:13	8	22:25:18	-01:49:07	p	
ecl01.06	1998 Sep 25	3:19 4:22 5:19	6	22:27:31	-03:12:49	p	
ecl01.05	1998 Sep 25	3:25 4:29 5:25	4	22:29:44	-04:36:29	p	
ecl01.03	1998 Sep 25	3:31 4:35 5:31	3	22:31:56	-06:00:00	m	
ecl01.02	1998 Sep 25	3:38 4:41 5:38	1	22:34:11	-07:38:00	m	
ecl01.00	1998 Sep 25	3:44 4:48 5:44	0	22:36:26	-08:47:00	m	
ecl07.00	1998 Sep 25	5:50 6:47 7:50	0	23:08:56	-05:28:00	p	
ecl07.01	1998 Sep 25	5:56 6:53 7:56	2	23:06:35	-04:05:00	m	
ecl07.03	1998 Sep 25	6:03 7:00 8:03	3	23:04:17	-02:42:00	m	
ecl08.03	1998 Sep 25	6:09 7:06 8:09	3	23:09:39	-02:09:00	p	
ecl08.01	1998 Sep 25	6:15 7:12 8:16	2	23:11:59	-03:31:00	m	
ecl08.00	1998 Sep 25	6:22 7:25 8:22	0	23:14:20	-04:54:00	p	
ecl09.00	1998 Sep 25	6:29 7:31 8:28	0	23:19:43	-04:20:00	p	
ecl09.01	1998 Sep 25	6:35 7:37 8:35	2	23:17:22	-02:57:00	p	
ecl09.03	1998 Sep 25	6:41 7:44 8:41	3	23:15:01	-01:34:00	p	
ecl25.00	1998 Sep 25	8:50 9:50 10:53	0	00:46:09	04:59:51	p	
ecl25.01	1998 Sep 25	8:56 9:56 10:59	2	00:43:48	06:20:15	p	
ecl25.03	1998 Sep 25	9:03 10:10 11:05	3	00:41:26	07:43:04	p	
ecl26.03	1998 Sep 25	9:10 10:17 11:11	3	00:46:56	08:17:41	p	
ecl26.01	1998 Sep 25	9:16 10:23 11:17	1	00:49:17	06:54:48	p	
ecl26.00	1998 Sep 25	9:22 10:29 11:23	0	00:51:38	05:31:52	p	
ecl27.00	1998 Sep 25	9:28 10:35 11:29	0	00:57:08	06:06:12	p	
ecl27.01	1998 Sep 25	9:37 10:41 11:35	1	00:54:47	07:29:13	p	
ecl27.03	1998 Sep 25	9:43 10:47 11:41	3	00:52:26	08:52:12	p	
ecl02.12	1998 Sep 26	2:36 3:33 4:29	12	22:23:58	02:53:28	m	
ecl02.11	1998 Sep 26	2:42 3:39 4:37	11	22:26:12	01:29:55	m	
ecl02.09	1998 Sep 26	2:48 3:45 4:43	9	22:28:25	00:06:19	g	
ecl02.08	1998 Sep 26	2:54 3:51 4:50	8	22:30:39	-01:17:15	g	
ecl02.06	1998 Sep 26	3:00 3:57 4:57	6	22:32:52	-02:40:49	m	

Table 3—Continued

ID	UT date	UT times	β ^a	α ^b	δ ^c	θ ^d	Objects
ecl02.05	1998 Sep 26	3:06 4:04 5:03	5	22:35:07	-04:04:21	m	
ecl02.03	1998 Sep 26	3:13 4:10 5:09	3	22:37:22	-05:27:55	g	
ecl02.02	1998 Sep 26	3:19 4:17 5:15	1	22:39:37	-06:51:22	m	
ecl02.00	1998 Sep 26	3:26 4:23 5:35	0	22:41:52	-08:14:50	m	
ecl10.00	1998 Sep 26	5:42 6:38 7:43	0	23:25:06	-03:45:45	m	
ecl10.01	1998 Sep 26	5:48 6:44 7:49	2	23:22:44	-02:23:02	m	
ecl10.03	1998 Sep 26	5:54 7:00 7:56	3	23:20:23	-01:00:15	g	
ecl11.03	1998 Sep 26	6:00 7:06 8:00	3	23:25:44	-00:25:49	g	
ecl11.01	1998 Sep 26	6:07 7:12 8:08	2	23:28:06	-01:48:33	g	1998 SN ₁₆₅
ecl11.00	1998 Sep 26	6:13 7:18 8:14	0	23:30:29	-03:11:16	g	
ecl12.00	1998 Sep 26	6:19 7:25 8:20	0	23:35:52	-02:36:35	g	
ecl12.01	1998 Sep 26	6:25 7:31 8:27	2	23:33:29	-01:13:53	m	
ecl12.03	1998 Sep 26	6:31 7:37 8:33	3	23:31:07	00:08:46	m	
ecl28.00	1998 Sep 26	8:39 9:49 10:50	0	01:02:37	06:40:22	m	
ecl28.01	1998 Sep 26	8:45 9:56 10:56	1	01:00:18	08:03:29	g	
ecl28.03	1998 Sep 26	8:59 10:02 11:02	3	00:57:58	09:26:32	m	
ecl29.03	1998 Sep 26	9:05 10:08 11:08	3	01:03:31	10:00:40	m	
ecl29.01	1998 Sep 26	9:12 10:14 11:15	1	01:05:50	08:37:32	m	
ecl29.00	1998 Sep 26	9:18 10:20 11:22	0	01:08:09	07:14:19	m	
ecl30.00	1998 Sep 26	9:24 10:26 11:28	0	01:13:41	07:48:03	m	
ecl30.01	1998 Sep 26	9:31 10:32 11:34	1	01:11:24	09:11:22	m	
ecl30.03	1998 Sep 26	9:37 10:38 11:40	3	01:09:05	10:34:40	g	
ecl31.00	1998 Sep 26	9:44 10:44 11:46	0	01:19:15	08:21:34	g	
ecl03.06	1998 Sep 27	2:26 3:26 4:36	6	22:38:15	-02:08:29	m	
ecl03.05	1998 Sep 27	2:32 3:33 4:42	4	22:40:30	-03:31:54	m	
ecl03.03	1998 Sep 27	2:38 3:39 4:48	3	22:42:44	-04:55:20	m	
ecl03.02	1998 Sep 27	2:44 3:51 4:56	2	22:45:01	-06:18:43	p	
ecl03.00	1998 Sep 27	2:50 3:57 5:02	0	22:47:18	-07:42:04	m	
ecl04.00	1998 Sep 27	2:56 4:04 5:08	0	22:52:44	-07:08:59	m	
ecl04.02	1998 Sep 27	3:02 4:10 5:14	1	22:50:26	-05:45:46	m	
ecl04.03	1998 Sep 27	3:08 4:16 5:20	3	22:48:09	-04:22:30	m	
ecl04.05	1998 Sep 27	3:14 4:22 5:26	5	22:45:52	-02:59:10	m	

Table 3—Continued

ID	UT date	UT times	β ^a	α ^b	δ ^c	θ ^d	Objects
ecl04.06	1998 Sep 27	3:20 4:30 5:33	6	22:43:37	-01:35:52		p
ecl13.00	1998 Sep 27	6:22 7:18 8:25	0	23:41:14	-02:01:50		p
ecl13.02	1998 Sep 27	6:28 7:24 8:31	1	23:38:52	-00:39:11		p
ecl13.03	1998 Sep 27	6:36 7:30 8:37	3	23:36:29	00:43:26		p
ecl14.03	1998 Sep 27	6:41 7:36 8:43	3	23:41:51	01:18:16		p
ecl14.02	1998 Sep 27	6:47 7:43 8:49	2	23:44:14	-00:04:20		p
ecl14.00	1998 Sep 27	6:53 7:49 8:55	0	23:46:37	-01:26:56		p
ecl15.00	1998 Sep 27	6:59 7:55 9:01	0	23:51:59	-00:51:59		p
ecl15.02	1998 Sep 27	7:05 8:02 9:07	1	23:49:37	00:30:35		p
ecl15.03	1998 Sep 27	7:11 8:09 9:13	3	23:47:14	01:53:11		m
ecl31.01	1998 Sep 27	9:28 10:23 11:17	1	01:16:59	09:45:00		p
ecl31.03	1998 Sep 27	9:34 10:29 11:23	3	01:14:40	11:08:23		p
ecl31.04	1998 Sep 27	9:42 10:35 11:36	5	01:12:21	12:31:42		p
ecl31.06	1998 Sep 27	9:48 10:41 11:42	6	01:10:01	13:54:55		p
ecl32.06	1998 Sep 27	9:53 10:47 12:13	6	01:15:39	14:28:38		p
ecl32.05	1998 Sep 27	9:59 10:53 11:49	5	01:17:59	13:05:18		p
ecl32.03	1998 Sep 27	10:05 10:59 11:55	3	01:20:17	11:41:53		p
ecl32.03	1998 Sep 27	10:11 11:05 12:01	2	01:22:34	10:18:22		p
ecl32.00	1998 Sep 27	10:17 11:11 12:07	0	01:24:50	08:54:49		m
ecl05.06	1998 Sep 28	2:21 3:37 4:37	6	22:48:57	-01:02:56		m
ecl05.05	1998 Sep 28	2:27 3:43 4:43	4	22:51:14	-02:26:12		m
ecl05.03	1998 Sep 28	2:33 3:49 4:49	3	22:53:32	-03:49:22		g
ecl05.02	1998 Sep 28	2:46 3:55 4:55	1	22:55:50	-05:12:33		g
ecl05.00	1998 Sep 28	2:52 4:01 5:01	0	22:58:08	-06:35:41		g
ecl06.00	1998 Sep 28	2:58 4:07 5:07	0	23:03:33	-06:02:07		g
ecl06.01	1998 Sep 28	3:04 4:13 5:13	2	23:01:13	-04:39:05		g
ecl06.03	1998 Sep 28	3:10 4:19 5:19	3	22:58:54	-03:15:59		m
ecl06.04	1998 Sep 28	3:16 4:25 5:25	4	22:56:36	-01:52:54		g
ecl06.06	1998 Sep 28	3:22 4:31 5:31	6	22:54:18	-00:29:46		g
e053m01.0	1999 Feb 15	10:00 10:54 11:50	-1	11:34:10	01:47:35		p
e053_00.0	1999 Feb 15	10:07 11:00 11:56	0	11:34:10	02:47:35		p
e053p01.0	1999 Feb 15	10:12 11:06 12:02	1	11:34:10	03:47:34		p

Table 3—Continued

ID	UT date	UT times	β ^a	α ^b	δ ^c	θ ^d	Objects
e054p01.0	1999 Feb 15	10:18 11:12 12:08	1	11:37:49	03:23:56		p
e054_00.0	1999 Feb 15	10:24 11:19 12:14	0	11:37:49	02:23:56		p
e054m01.0	1999 Feb 15	10:30 11:26 12:20	-1	11:37:50	01:23:53		p
e055m01.0	1999 Feb 15	10:36 11:32 12:26	-1	11:41:29	01:00:13		p
e055_00.0	1999 Feb 15	10:42 11:38 12:32	0	11:41:29	02:00:13		p
e055p01.0	1999 Feb 15	10:48 11:45 12:38	1	11:41:29	03:00:13		p
e013p02.0	1999 Feb 20	3:14 4:33 5:45	2	09:00:36	19:00:04		m
e013p01.0	1999 Feb 20	3:20 4:40 5:51	1	09:00:36	18:00:07		m
e013_00.0	1999 Feb 20	3:26 4:46 5:57	0	09:00:36	17:00:06		m
e013m02.0	1999 Feb 20	3:32 4:52 6:03	-2	09:00:36	15:00:06		g
e016m01.0	1999 Feb 20	3:37 4:58 6:09	-1	09:12:45	15:07:18		m
e016_00.0	1999 Feb 20	3:43 5:04 6:15	0	09:12:45	16:07:17		g
e016p01.0	1999 Feb 20	3:49 5:10 6:21	1	09:12:45	17:07:18		m
e016p02.0	1999 Feb 20	3:55 5:16 6:27	2	09:12:45	18:07:18		m
e023p02.0	1999 Feb 20	4:01 5:22 6:33	2	09:40:39	15:54:37		m
e023p01.0	1999 Feb 20	4:07 5:28 6:39	1	09:40:39	14:54:36		g
e023_00.0	1999 Feb 20	4:13 5:33 6:45	0	09:40:39	13:54:37		m
e023m01.0	1999 Feb 20	4:19 5:39 6:51	-1	09:40:39	12:54:35		g
e032m01.0	1999 Feb 20	6:57 8:10 9:21	-1	10:15:38	09:47:45	g	1999 DE ₉
e032_00.0	1999 Feb 20	7:03 8:16 9:27	0	10:15:38	10:47:45	g	
e032p01.0	1999 Feb 20	7:09 8:22 9:33	1	10:15:38	11:47:45	g	1999 DF ₉
e032p02.0	1999 Feb 20	7:15 8:28 9:39	2	10:15:38	12:47:44	g	
e040m01.0	1999 Feb 20	7:46 8:58 10:22	-1	10:45:58	06:50:10		g
e040_00.0	1999 Feb 20	7:52 9:03 10:28	0	10:45:58	07:50:11		g
e040p01.0	1999 Feb 20	7:58 9:09 10:34	1	10:45:58	08:50:11		g
e040p02.0	1999 Feb 20	8:04 9:15 10:40	2	10:45:58	09:50:11		g
e047m01.0	1999 Feb 20	10:46 11:36 12:12	-1	11:12:03	04:08:46		g
e047_00.0	1999 Feb 20	10:52 11:42 12:18	0	11:12:03	05:08:45		m
e047p01.0	1999 Feb 20	10:58 11:48 12:25	1	11:12:03	06:08:46		g
e1002p05	2000 Mar 03	3:06 4:22 5:31	5	09:24:33.7	20:18:02.1		g
e1002p04	2000 Mar 03	3:19 4:28 5:37	4	09:24:33.7	19:17:02.0		g
e1002p03	2000 Mar 03	3:25 4:35 5:44	3	09:24:33.7	18:16:01.9		g

Table 3—Continued

ID	UT date	UT times	β ^a	α ^b	δ ^c	θ ^d	Objects
e1002p02	2000 Mar 03	3:31 4:41 5:50	2	09:24:33.7	17:15:01.8	g	
e1002p01	2000 Mar 03	3:37 4:47 5:57	1	09:24:33.7	16:14:01.6	g	
e1002_00	2000 Mar 03	3:44 4:53 6:03	0	09:24:33.7	15:13:01.5	g	
e1002m01	2000 Mar 03	3:50 5:00 6:10	-1	09:24:33.7	14:12:01.4	g	
e1002m02	2000 Mar 03	3:57 5:06 6:15	-2	09:24:33.7	13:11:01.3	g	
e1002m03	2000 Mar 03	4:03 5:12 6:22	-3	09:24:33.7	12:10:01.2	g	2000 EE ₁₇₃
e1002m04	2000 Mar 03	4:09 5:18 6:28	-4	09:24:33.7	11:09:01.0	g	
e1002m05	2000 Mar 03	4:15 5:25 6:34	-5	09:24:33.7	10:08:00.9	g	
e1020m05	2000 Mar 03	6:42 7:51 9:00	-5	10:40:33.6	03:17:43.3	g	
e1020m04	2000 Mar 03	6:48 7:57 9:06	-4	10:40:33.6	04:18:43.4	g	
e1020m03	2000 Mar 03	6:54 8:03 9:13	-3	10:40:33.6	05:19:43.5	g	
e1020m02	2000 Mar 03	7:00 8:10 9:19	-2	10:40:33.6	06:20:43.6	g	
e1020m01	2000 Mar 03	7:07 8:16 9:26	-1	10:40:33.6	07:21:43.8	g	
e1020_00	2000 Mar 03	7:13 8:22 9:32	0	10:40:33.6	08:22:43.9	g	
e1020p01	2000 Mar 03	7:19 8:28 9:38	1	10:40:33.6	09:23:44.0	g	
e1020p02	2000 Mar 03	7:24 8:35 9:45	2	10:40:33.6	10:24:44.1	g	
e1020p03	2000 Mar 03	7:32 8:41 9:51	3	10:40:33.6	11:25:44.2	g	
e1020p04	2000 Mar 03	7:38 8:47 9:57	4	10:40:33.6	12:26:44.4	g	
e1020p05	2000 Mar 03	7:45 8:54 10:03	5	10:40:33.6	13:27:44.5	g	
e1041m05	2000 Mar 03	10:11 10:56 11:55	-5	12:05:04.3	-05:37:58.9	m	
e1041m04	2000 Mar 03	10:17 11:03 12:01	-4	12:05:04.3	-04:36:58.8	g	
e1041m03	2000 Mar 03	10:23 11:09 12:08	-3	12:05:04.3	-03:35:58.6	g	
e1003m05	2000 Mar 04	2:28 3:44 4:47	-5	09:28:54.5	09:47:19.9	m	
e1003m04	2000 Mar 04	2:34 3:50 4:54	-4	09:28:54.5	10:48:20.0	p	
e1003m03	2000 Mar 04	2:40 3:57 5:06	-3	09:28:54.5	11:49:20.1	m	
e1003m01	2000 Mar 04	2:59 4:03 5:13	-1	09:28:54.5	13:51:20.4	m	
e1003_00	2000 Mar 04	3:05 4:10 5:20	0	09:28:54.5	14:52:20.5	m	
e1003p01	2000 Mar 04	3:13 4:16 5:26	1	09:28:54.5	15:53:20.6	m	
e1003p02	2000 Mar 04	3:19 4:22 5:32	2	09:28:54.5	16:54:20.7	m	
e1003p03	2000 Mar 04	3:25 4:29 5:38	3	09:28:54.5	17:55:20.8	m	
e1003p04	2000 Mar 04	3:32 4:35 5:45	4	09:28:54.5	18:56:21.0	m	
e1003p05	2000 Mar 04	3:38 4:41 5:51	5	09:28:54.5	19:57:21.1	g	

Table 3—Continued

ID	UT date	UT times	β ^a	α ^b	δ ^c	θ ^d	Objects
e1021m04	2000 Mar 04	5:58 6:55 8:14	-4	10:44:39.7	03:54:03.5	m	
e1021m03	2000 Mar 04	6:04 7:01 8:20	-3	10:44:39.7	04:55:03.6	m	
e1021m02	2000 Mar 04	6:10 7:07 8:27	-2	10:44:39.7	05:56:03.7	m	
e1021m01	2000 Mar 04	6:16 7:25 8:33	-1	10:44:39.7	06:57:03.8	m	
e1021_00	2000 Mar 04	6:23 7:32 8:39	0	10:44:39.7	07:58:04.0	m	
e1021p01	2000 Mar 04	6:29 7:40 8:45	1	10:44:39.7	08:59:04.1	p	
e1021p02	2000 Mar 04	6:35 7:46 8:52	2	10:44:39.7	10:00:04.2	p	
e1021p03	2000 Mar 04	6:41 7:52 8:58	3	10:44:39.7	11:01:04.3	p	
e1035p05	2000 Mar 04	9:26 10:17 11:10	5	11:41:11.8	07:07:06.2	m	
e1036p05	2000 Mar 04	9:32 10:23 11:17	5	11:45:11.1	06:41:15.9	m	
e1037p05	2000 Mar 04	9:39 10:29 11:23	5	11:49:10.1	06:15:24.8	p	

Note. — This table lists fields imaged with the KPNO 8k Mosaic camera. Fields were imaged in triplets, with UT times given for each image. KBOs found are listed after the field of discovery. The complete version of this table is in the electronic edition of the Journal. The printed edition contains only a sample.

^aJ2000 ecliptic latitude, degrees

^bJ2000 right ascension, hours

^cJ2000 declination, degrees

^dSeeing category: g, m, p represent the good (< 1.5 arc sec), medium (≥ 1.5 arc sec and < 2.0 arc sec), and poor (≥ 2.0 arc sec) seeing cases, respectively. The efficiency functions for each of these cases are presented in Table 4.

Table 4. KPNO Survey Efficiency

	Good	Medium	Poor	Global
Median PSF FWHM ["]	1.3	1.6	2.1	1.5
PSF FWHM Range ["]	1.0–1.4	1.5–1.9	2.0–2.4	1.0–2.4
e_{\max}	0.88	0.88	0.80	0.85
m_{R50}	21.4	21.2	20.8	21.1
σ	0.5	0.5	0.4	0.6
Fields Imaged	57	61	53	171
Total Area [deg ²]	55	58	51	164
KBOs	3	0	0	3
Centaurs	1	0	0	1

Note. — Survey efficiency for three seeing cases and “Global” efficiency, representing the sky-area weighted mean of the three efficiencies, designed to represent the properties of the KPNO data set in its entirety.

Table 5. The KPNO Objects

	1998 SN ₁₆₅ ^a	1999 DE ₉	1999 DF ₉	2000 EE ₁₇₃
Discovery Conditions				
Date	1998 Sep 26	1999 Feb 20	1999 Feb 20	2000 Mar 03
R [AU]	38.248	32.549	39.765	23.593
Δ [AU]	37.264	33.537	38.776	22.678
α' [deg]	0.3	0.0	0.0	0.9
m_R	21.2 ± 0.1	19.7 ± 0.1	21.6 ± 0.1	22.2 ± 0.1
$m_R(1, 1, 0)$	5.4	4.5	5.7	8.4
Diameter [km]	480	710	420	120
a [AU]	37.900 ± 0.003	56.4 ± 0.5	46.400 ± 0.053	49.02 ± 0.06
e	0.0437 ± 0.0004	0.435 ± 0.009	0.144 ± 0.004	0.5387 ± 0.0007
i [deg]	4.605 ± 0.0005	7.623 ± 0.002	9.819 ± 0.005	5.950 ± 0.0004
Ω (node) [deg]	192.097 ± 0.002	322.983 ± 0.003	334.856 ± 0.002	294.070 ± 0.002
ω (peri) [deg]	264.156 ± 0.145	155.7 ± 1.7	169 ± 11	235.05 ± 0.13
τ (time of peri) [JD]	2474593 ± 36	2445972 ± 222	2449415 ± 2573	2454160 ± 10
epoch	2451071.7	2451229.8	2451229.8	2451606.7
perihelion	36.33554	31.83661	39.70701	22.62496

Note. — Discovery conditions of the objects found in this survey. R is the heliocentric distance. Δ is geocentric distance. α' is phase angle. m_R is the red magnitude at discovery. $m_R(1, 1, 0)$ is red magnitude at zero phase angle, with heliocentric and geocentric distance = 1 AU. The diameter is derived assuming a geometric albedo of 4%. Orbital elements and associated errors were computed using the procedure of Bernstein and Khushalani (2000) with data provided by the Minor Planet Center.

^aThis object was discovered by Spacewatch on Sep 23, 1998 and serendipitously detected in our data.

Table 6. Classical KBO Model Assumptions

Quantity	Value	Distribution	Description
a [AU]	$41 < a < 47$	$n(a)da \sim a^{1-p}da$	semimajor axis distribution
p^a	2	—	semimajor axis power
q'^b [AU]	$q' < 37.0$	—	perihelion criterion
i	—	Gaussian	inclination distribution
$i_{1/2}^c$ [deg]	20.0	—	inclination half-width
r [km]	$25 < r < 16000$	$n(r)dr \sim r^{-q}dr$	radius distribution
q	fitted	—	radius distribution power
$N_{\text{CKBOs}}(D > 100 \text{ km})$	fitted	—	number of CKBOs with $D > 100 \text{ km}$
N_{bins}	50	logarithmic	number of radius bins

^aFor circular orbits, p represents the decrease in ecliptic plane surface density Σ_{ecl} as a function of heliocentric distance R , $\Sigma_{\text{ecl}} \sim R^{-p}$.

^bEccentricity assumed to be uniform between 0 and 1 consistent with perihelion criterion.

^cBest-fit values from Trujillo, Jewitt & Luu (2001).

Table 7. Objects Brighter than 20 R

	1996 GQ ₂₁	1999 DE ₉	2000 EB ₁₇₃
Discovery Conditions			
Date	1996 Apr 12	1999 Feb 20	2000 Mar 10
R [AU]	38.523	32.549	29.940
Δ [AU]	37.521	33.537	29.036
α' [deg]	0.1	0.0	0.8
m	20.5 V	19.7 R	19.3 R
$m(1, 1, 0)$	4.7 V	4.5 R	4.5 R
Diameter [km]	720	710	780
a [AU]	94.06 ± 0.10	56.4 ± 0.5	39.22 ± 0.03
e	0.5955 ± 0.0007	0.435 ± 0.009	0.2697 ± 0.0011
i [deg]	13.357 ± 0.003	7.623 ± 0.002	15.476 ± 0.0004
Ω (node) [deg]	194.184 ± 0.0003	322.983 ± 0.003	169.331 ± 0.001
ω (peri)[deg]	353.992 ± 0.3	155.7 ± 1.7	66.8 ± 0.2
τ (time of peri) [JD]	2447365 ± 54	2445972 ± 222	2456944 ± 22
epoch [JD]	2450185.8	2451229.8	2450182.7
source	Larsen et al. (2001)	This Work	Ferrin et al. (2001)

Note. — Discovery conditions of all KBOs brighter than 20 R discovered in published surveys (Pluto excepted). R is the heliocentric distance. Δ is geocentric distance. m is the magnitude at discovery. $m(1, 1, 0)$ is magnitude at zero phase angle, with geocentric and heliocentric distance = 1 AU. The diameter is derived assuming a geometric albedo of 4%. Orbital elements and associated errors were computed using the procedure of Bernstein and Khushalani (2000) with data provided by the Minor Planet Center.